JACS Au
AN OPEN ACCESS JOURNAL OF THE AMERICAN CHEMICAL SOCIETY

pubs.acs.org/jacsau

Article

Time-Resolved Local pH Measurements during CO_2 Reduction Using Scanning Electrochemical Microscopy: Buffering and Tip Effects

Mariana C. O. Monteiro, Alex Mirabal, Leon Jacobse, Katharina Doblhoff-Dier, Scott Calabrese Barton, and Marc T. M. Koper*

Cite This: *JACS Au* 2021, 1, 1915–1924

Read Online

ACCESS | Metrics & More | Article Recommendations | Supporting Information

ABSTRACT: The electrochemical reduction of CO_2 is widely studied as a sustainable alternative for the production of fuels and chemicals. The electrolyte's bulk pH and composition play an important role in the reaction activity and selectivity and can affect the extent of the buildup of pH gradients between the electrode surface and the bulk of the electrolyte. Quantifying the local pH and how it is affected by the solution species is desirable to gain a better understanding of the CO_2 reduction reaction. Local pH measurements can be realized using Scanning Electrochemical Microscopy (SECM); however, finding a pH probe that is stable and selective under CO_2 reduction reaction conditions is challenging. Here, we have used our recently developed voltammetric pH sensor to perform pH measurements in the diffusion layer during CO_2 reduction using SECM, with high time resolution. Using a 4-hydroxylaminothiophenol (4-HATP)/4-nitrosothiophenol (4-NSTP) functionalized gold ultramicroelectrode, we compare the local pH developed above a gold substrate in an argon atmosphere, when only hydrogen evolution is taking place, to the pH developed in a CO_2 atmosphere. The pH is monitored at a fixed distance from the surface, and the sample potential is varied in time. In argon, we observe a gradual increase of pH, while a plateau region is present in CO_2 atmosphere due to the formation of HCO_3^- buffering the reaction interface. By analyzing the diffusion layer dynamics once the sample reaction is turned "off", we gain insightful information on the time scale of the homogeneous reactions happening in solution and on the time required for the diffusion layer to fully recover to the initial bulk concentration of species. In order to account for the effect of the presence of the SECM tip on the measured pH, we performed finite element method simulations of the fluid and reaction dynamics. The results show the significant localized diffusion hindrance caused by the tip, so that in its absence, the pH values are more acidic than when the tip is present. Nonetheless, through the simulation, we can account for this effect and estimate the real local pH values across the diffusion layer.

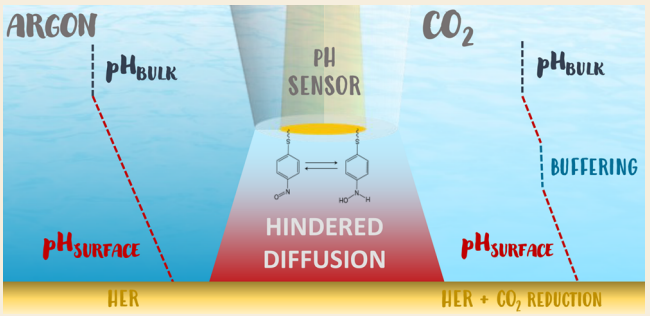

KEYWORDS: *CO_2 electroreduction, local pH, SECM, buffering, finite element method*

INTRODUCTION

The electrochemical conversion of CO_2 to higher-added-value products has gained attention in the past years as a potential pathway toward replacing fossil fuels as feedstock. In aqueous media, the reduction of CO_2 (CO_2RR) competes with the hydrogen evolution reaction (HER), and activity and selectivity are key factors to make this process viable at industrially relevant scales.[1] In order to steer the selectivity and improve the overall reaction energetics, most studies focus on the catalyst material.[2,3] However, another efficient way of tuning CO_2RR is through the electrolyte composition.[4,5] By changing the electrolyte's buffer capacity,[6−8] pH,[9−11] cation,[12−15] or anion,[16,17] one can strongly influence the rate and selectivity of the reaction. However, understanding and decoupling these electrolyte effects is necessary in order to optimize the reaction via these variables.

In many studies, the activity for CO_2 reduction is assessed without actual knowledge of the interfacial pH, which can vary drastically from the bulk depending on the current density, electrolyte buffer capacity, and diffusion coefficient of the species in solution. On gold, at low overpotentials, CO_2RR and HER yield mainly carbon monoxide (CO) and hydrogen (H_2) through the following reactions:[18]

$$CO_2 + H_2O + 2e^- \leftrightarrow CO + 2OH^- \quad (1)$$

Received: June 26, 2021
Published: October 13, 2021

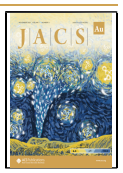

https://doi.org/10.1021/jacsau.1c00289
JACS Au 2021, 1, 1915–1924

$$2H^+ + 2e^- \leftrightarrow H_2 \quad (2)$$

$$2H_2O + 2e^- \leftrightarrow H_2 + 2OH^- \quad (3)$$

The interfacial pH and the overpotential will determine whether the overall HER current is dominated by proton or water reduction, as displayed in eqs 2 and 3, respectively. Because of the consumption of protons or formation of OH^- by both HER and CO_2RR, the pH near the electrode surface can drastically vary from the bulk pH. Apart from reactions 1−3, various homogeneous reactions may take place in the CO_2-water system as a function of pH:[19]

$$CO_2 + H_2O \leftrightarrow H_2CO_3 \quad (4)$$

$$H_2CO_3 \leftrightarrow HCO_3^- + H^+ \quad pK_a = 3.6 \quad (5)$$

$$CO_2 + OH^- \leftrightarrow HCO_3^- \quad pK_a = 6.4 \quad (6)$$

$$HCO_3^- + OH^- \leftrightarrow CO_3^{2-} \quad pK_a = 10.3 \quad (7)$$

$$H_2O \leftrightarrow H^+ + OH^- \quad pK_a = 14.0 \quad (8)$$

Quantifying the pH gradients formed in the diffusion layer during CO_2RR is crucial in order to gain a better understanding of the reaction. Even though various techniques are available for measuring local pH in electrochemistry,[20] directly measuring the pH in the diffusion layer during CO_2 reduction is challenging. This is due to the complex reaction environment and the fact that the signal and stability of the pH probe should not be affected by the reactants, products, or the electrolyte identity. To date, pH measurements during CO_2 reduction under stationary conditions have been mainly achieved using spectroscopic techniques. Yang et al.,[21] for instance, used surface enhanced infrared absorption spectroscopy (SEIRAS) to determine the pH near the surface during CO_2RR on sputtered copper thin films by monitoring the change in signal intensity of the species composing the phosphate buffer used ($H_2PO_4^-$/ HPO_4^{2-}/ PO_4^{3-}). Results showed that even in strongly buffered electrolyte, the pH near the surface differs from the bulk at current densities lower than 10 mA cm^{-2}. Ayemoba et al.[22] probed the pH during CO_2RR on gold thin films using surface-enhanced infrared absorption spectroscopy in the attenuated total reflection mode (ATR-SEIRAS). In this case, the ratio between the integrated absorbance of the CO_2 and HCO_3^- bands was used to estimate the pH near the surface. Similar measurements, were recently reported in a flow cell using Raman spectroscopy.[23] Although, in general, these spectroscopic techniques can provide valuable information about the concentration of species in the first few nanometres above the surface, the signal obtained is averaged over a large surface area. Furthermore, these measurements require having infrared or Raman active species in solution, and the pH is measured indirectly—by monitoring species whose signal is a function of the proton concentration. If these species are also affected by other variables of the reaction environment, the signal might be a convolution thereof. Therefore, spectroscopic techniques can be limited in terms of electrode materials and electrolytes that can be employed. As an alternative to spectroscopy, Zhang et al.[24] have recently used the rotating ring-disc electrode technique to measure changes in pH during CO_2 reduction on gold under mass transport control. In this case, a correlation between potentiometric pH measurements with IrOx and shifts in the CO oxidation peak detected with a Pt ring were used to determine the disc pH. Even though this allows for pH measurements under mass transport control, the method is limited in terms of temporal (when IrOx is used) and spatial resolution (similarly to spectroscopic techniques). Additionally, even though the CO signal on platinum is used as a pH probe, it is known that this reaction is affected not only by pH[25] but also cation identity[26] or surface structure.[27]

Scanning Electrochemical Microscopy (SECM) allows for performing pH measurements with high spatial and temporal resolution. The spatial resolution is only limited by the tip size, and the temporal resolution depends on the pH probe used. SECM also offers high versatility in terms of substrate (gas diffusion, flat, thin film electrodes) and pH sensors (potentiometric, voltammetric) that can be used. However, finding a pH probe that is not destabilized by the CO_2 reduction reaction environment can be challenging. For example, commonly used (in both SECM and RRDE) potentiometric pH sensors such as IrO_x or Pt can strongly interact with CO. This can generate a convoluted open circuit potential response, hindering the applicability of these materials to measure pH during CO_2RR. Using gas diffusion electrodes (GDEs) operating at high current densities, Dieckenhöfer et al.[28] overcame this problem by collecting the products at the back of the GDE, so as to avoid CO getting in contact with the SECM Pt tip. Unfortunately, the pH response of the platinum nanoelectrode is only applicable in highly alkaline environments, as evident from the calibration curve reported by the authors in 1 to 16 M KOH solutions. Such a high alkalinity at the interface can only be achieved when using high turnover substrates (highly porous electrodes, GDEs) or when operating at high overpotentials. This means that this Pt sensor cannot be used to investigate CO_2RR on less porous substrates or in neutral/acidic conditions. With that in mind, we have recently developed a highly stable, selective, and sensitive SECM pH probe based on the functionalization of gold ultramicroelectrodes (Au-UMEs) with a 4-nitrothiophenol self-assembled monolayer.[29] Contrary to the commonly used IrO_x, this voltammetric pH probe can provide high temporal resolution, only dependent on the scan rate applied at the tip, showing a stable pH response in a wide pH range. Additionally, the fact that the sensor is formed by a monolayer on the tip surface, overcomes time response issues often encountered when using either a polymer or solid oxide film.

Our modified Au-UME pH sensor is employed in this work to perform and compare direct pH measurements during HER and CO_2RR on polycrystalline gold. We monitor the evolution of pH in time while stepping the electrode potential in either argon or CO_2 atmosphere. Our results show that the homogeneous reactions involving CO_2 in aqueous media are sufficient to buffer the reaction interface to a certain extent, in spite of using an otherwise unbuffered electrolyte. The high sensitivity and time resolution of our pH probe enables us to analyze the dynamics of the diffusion layer pH as a function of the species present in solution, which has not been previously reported for CO_2 reduction using SECM. Additionally, in this work, we have accounted for the effect of the SECM tip on the diffusion layer concentration fields, and consequently on the pH measured for CO_2RR and HER, using 2D, dynamic transport and reaction simulations based on finite element methods (FEM). Simulations are fitted to experimental results to estimate kinetic parameters and enable further analysis of SECM tip effects relevant to the experimental system. This

https://doi.org/10.1021/jacsau.1c00289
JACS Au 2021, 1, 1915−1924

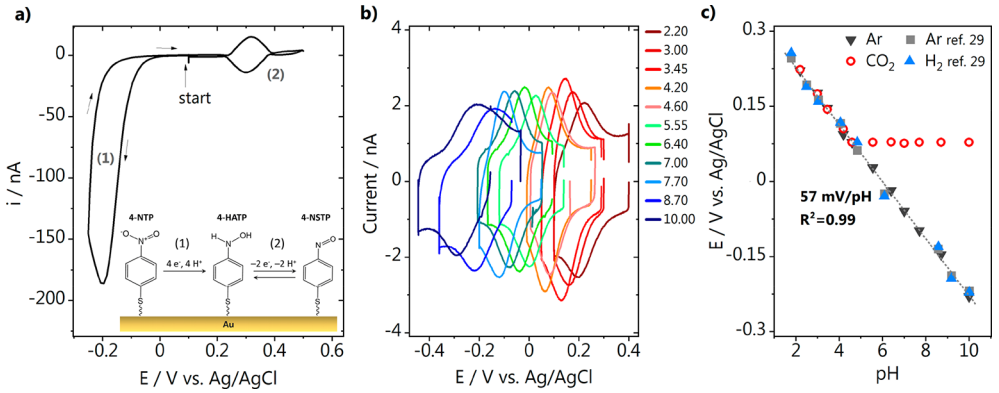

Figure 1. SECM pH sensor synthesis and calibration. (a) Voltammogram of the functionalized Au-UME showing the conversion of 4-nitrothiophenol (4-NTP) to the pH sensitive redox couple 4-hydroxylaminothiophenol (4-HATP)/4-nitrosothiophenol(4-NTP); (b) pH sensor voltammetry in 0.1 M Li_2SO_4 solutions adjusted to different pH, taken at 200 mV s^{-1}; (c) Calibration curves of the modified Au-UME pH sensor in different gaseous atmospheres. The calibration curves from our previous work (ref 29) are also shown for comparison.

work brings pH measurements during CO_2 reduction one step further, by showing that it can be realized using SECM, with high time resolution and over a wide pH range. This allows for decoupling the pH effect from other electrolyte/surface effects on the reaction in future studies.

RESULTS AND DISCUSSION

pH Sensor Synthesis and Calibration

The gold ultramicroelectrodes (Au-UMEs) are first characterized by blank voltammetry in 0.1 M H_2SO_4 in order to ensure good sealing and surface cleanliness. A cyclic voltammogram characterizing the Au-UME (25 μm radius) used in this study can be seen in Figure S1 in the Supporting Information (SI). In order to perform the SECM pH measurements, the Au-UME is functionalized with the 4-hydroxylaminothiophenol/4-nitrosothiophenol redox couple. This is done by immersion of the Au-UME in a solution containing 4-nitrothiophenol (4-NTP), which leads to the self-assembly of this organic molecule on the Au-UME surface. Next, 4-NTP is partially[30] electrochemically reduced to 4-hydroxylaminothiophenol (4-HATP) in 0.1 M H_2SO_4, as depicted in Figure 1a. The cathodic potential limit must be carefully controlled in order to maximize the conversion to 4-HATP and minimize the amount of 4-aminothiophenol (4-ATP) formed. On the positive-going scan, an anodic peak can be seen in the gold double layer region between 0.2 and 0.4 V vs Ag/AgCl due to oxidation of 4-HATP, forming 4-nitrosothiophenol (4-NSTP). This is a highly reversible reaction, demonstrated by the subsequent symmetrical cathodic current in the negative-going scan. A schematic representation of the reactions taking place at the Au-UME surface can be seen in the inset of Figure 1a, which is correlated to the voltammetry of (1) the reduction of 4-NTP to 4-HATP and (2) the 4-HATP/4-NSTP redox couple.

The calibration of the functionalized Au-UME pH sensor is performed in the same electrolyte the SECM measurements are carried out, but in different gaseous atmospheres. The cyclic voltammetry (CV) of the tip is recorded in 0.1 M Li_2SO_4 solutions adjusted to different pH and saturated with either argon or CO_2. The CVs obtained in argon are shown in Figure 1b and the ones recorded in CO_2 saturated electrolyte can be found in Figure S2 in the SI. The midpeak potential of the 4-HATP/4-NSTP anodic voltammetry is obtained through a Gaussian fit (with a linear background) of the CVs and can be used to construct the calibration curve shown in Figure 1c. Because of the reversible oxidation and reduction of the 4-HATP/4-NSTP involving two protons and two electrons, a Nernstian response is obtained with a shift of 57 mV/pH unit and an R^2 of 0.99. The calibration curves in argon and CO_2 atmosphere overlap until pH 3.45. This is expected as at higher pH values, carbonic acid is formed and the CO_2 saturated solutions equilibrate at a constant pH around 4 (see eqs 4 and 5). We have also displayed the calibration curves presented in our previous work[29] in Figure 1c, which show how reproducible the pH sensor response is when comparing different measurements, performed in different gaseous atmospheres.

SECM Measurements

Once the Au-UME is functionalized, the tip is positioned at a certain distance to the sample using a capacitive approach in air, which was introduced in our previous work.[25,29,31] In short: an AC potential is applied to the sample while the capacitive current generated at the tip is recorded. The capacitance is plotted as a function of distance from the surface (Figure S3) and behaves exponentially at small tip-to-surface distances. The fitting of the approach curve with eq 9 (see Experimental Section) is used to determine the absolute surface position. Before performing the SECM pH measurements, the cyclic voltammetry of HER and CO_2RR taking place at the polycrystalline gold sample in 0.1 M Li_2SO_4 (pH_{bulk} = 3) was recorded (Figure 2). In argon atmosphere, a large cathodic current is observed at potentials more negative than −0.4 V vs Ag/AgCl because of the reduction of protons. The reaction becomes diffusion limited due to the depletion of protons at the interface, and consequently, in the subsequent four cycles, a significantly lower proton reduction current is observed. In the presence of CO_2, proton reduction and CO_2 reduction take place in parallel, but a larger current is observed only at potentials more negative than −1 V vs Ag/AgCl, suggesting that the contribution of CO_2 reduction to the current observed at more positive potentials is minimal. The first cycle overlaps with the CV taken in argon atmosphere, as the starting bulk pH is the same, however larger currents are obtained in the subsequent four cycles in CO_2 atmosphere. The latter indicates that the alkalinity near surface is lower in the presence of CO_2. However, cyclic voltammetry can only provide qualitative information about the proton concentration near the surface.

https://doi.org/10.1021/jacsau.1c00289
JACS Au 2021, 1, 1915−1924

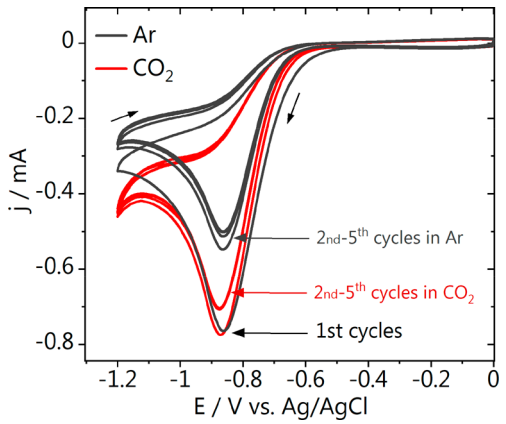

Figure 2. CVs in argon (black) and CO_2 (red) atmosphere taken at the gold sample in 0.1 M Li_2SO_4 (pH = 3, 100 mV s^{-1}).

To quantify the changes in pH in the diffusion layer during these reactions using SECM, the functionalized Au-UME pH sensor is placed at a constant distance of 80 ± 2 μm from the gold surface. The reactions are turned "on" and "off" by stepping the sample potential from −0.5 to −0.9 V vs Ag/AgCl in 50 mV steps. In between potential steps, the gold substrate is held at 0 V. The tip voltammetry is constantly recorded at 200 mV s^{-1}, which allows capturing the changes in pH with high time resolution (4 s/data point). Figure 3a shows the results obtained in argon atmosphere (gray triangles) and then in CO_2 atmosphere (red circles). These data were obtained in two consecutive measurements and are plotted on top of each other to facilitate comparison. The peak potentials obtained from fitting the 4-HATP/4-NSTP voltammetry (used to extract these pH data) and the current recorded at the sample during the chronoamperometry can be found in Figure S4 and Figure S5 in the SI. From the results in Figure 3a, it can be seen that at low overpotentials and consequently low current densities (between −0.5 and −0.6 V), small pH changes of maximum 1.5 pH unit are observed at the interface, both in argon and CO_2 atmosphere. At these potentials (and pH) proton reduction is the main reaction taking place, and the activity for CO_2RR is still quite low. Although proton reduction is kinetically limited in this narrow potential window, the low proton bulk concentration (pH 3), explains the relatively small effect on the measured pH. The significant pH change we observe even when the reaction appears kinetically limited is related to the presence of the tip, which inhibits local mass transport, as we will later illustrate in the Finite Element Method (FEM) Simulations section. Between −0.65 and −0.9 V vs Ag/AgCl, however, the pH recorded in argon atmosphere gradually increases as a function of potential. At these higher interfacial pH values, hydrogen is produced through the reduction of water. As water reduction is a kinetically limited reaction producing OH^-, the alkalinity is expected to increase with the potential. In CO_2 atmosphere, between −0.65 and −0.8 V vs Ag/AgCl, we observe that the pH does not significantly increase as the potential is scanned more negatively, although we work in an unbuffered electrolyte. When the pH at the interface becomes alkaline, the reversible reaction between CO_2 and HCO_3^- (pK_a = 6.4, eq 6) seems to takes place fast enough, so that the CO_2 supplied not only is a reactant but also acts as a buffer to a certain extent. Once potentials more negative than −0.8 V are applied, there is a buffer "breakdown" and the pH increases more than a unit above the pK_a of the CO_2/HCO_3^- reversible reaction. In fact, this buffering can also be observed in CO_2 atmosphere at lower overpotentials, where the maximum pH reached is still below 6. Interestingly, as shown in Figure 3b, once the reaction is turned "on", there is first an increase in pH that reaches a maximum value after 30−35 s. Subsequently, the pH decreases as the OH^- produced are neutralized by the forward CO_2/HCO_3^- reaction (eq 6).

Going one step further than in our previous work,[25] here the dynamics of the CO_2-derived species in the diffusion layer was investigated by focusing on the relaxation of the pH after the potential is returned to 0 V, in the presence and absence of CO_2. Figure 4a,b show the time evolution of the pH measured at the tip once the sample reaction is turned "off", after the different potentials shown in Figure 3a are applied to the sample. It can be seen in Figure 4a that in argon atmosphere, once HER is turned "off", for nearly all sample potentials the pH drops to values below 4.5 within 5 s. Only when the reaction is carried out at −0.9 V it takes slightly longer, but no more than 10 s. For low sample overpotentials, the interfacial pH returns to bulk pH within 25 s and even at the higher

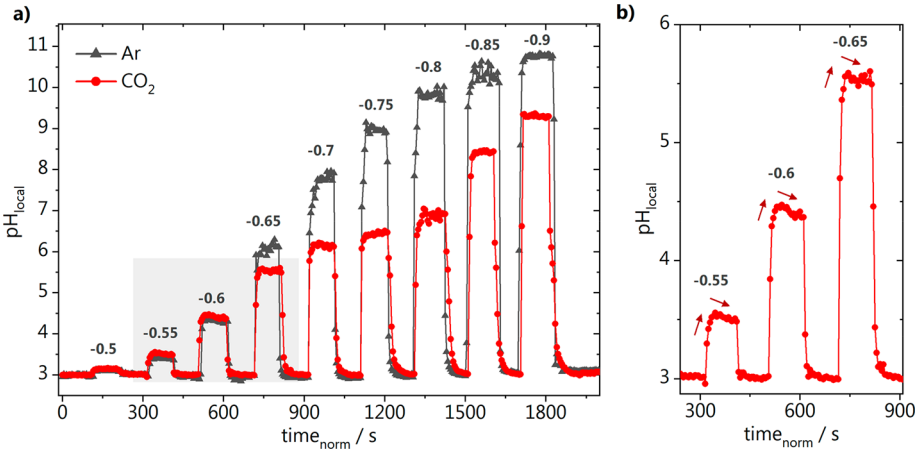

Figure 3. Local pH measured in time. (a) Comparison of the pH measured at the same distance from the surface in argon and CO_2 atmosphere; (b) inset of the shaded area of panel a showing the pH trend at low overpotentials. The sample potentials are indicated on top of the curves, in V vs Ag/AgCl.

https://doi.org/10.1021/jacsau.1c00289
JACS Au 2021, 1, 1915−1924

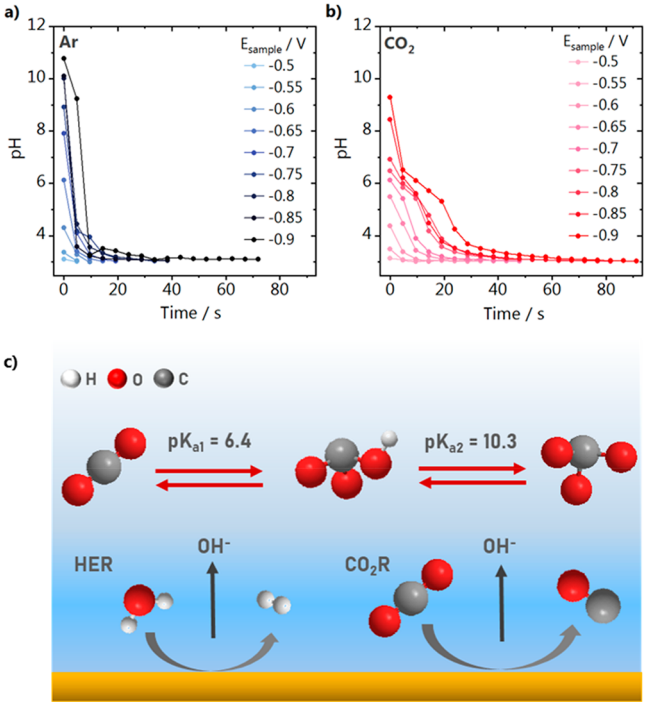

Figure 4. Diffusion layer dynamics: pH recovery in the diffusion layer when (a) hydrogen evolution and (b) CO_2 reduction are turned "off". Sample potentials are reported versus Ag/AgCl. (c) Schematic representation of the homogeneous reactions taking place in solution in parallel to the electrocatalytic reactions.

overpotentials this takes only 35 s. A very different behavior is observed in CO_2 atmosphere as a function of sample potential, and consequently local pH, as shown in Figure 4b. Here, the time for returning to the bulk pH value increases gradually with the sample potential applied, which modulates the local pH, and consequently, the concentration of species in equilibrium in solution. At potentials more positive than −0.65 V, the pH decreases gradually and equals the bulk pH 25 s after the reaction is turned "off" (similarly to argon). At intermediate sample potentials (−0.7 to −0.8 V), the initial near-surface pH is above the pK_a of the CO_2/HCO_3^- equilibrium, and therefore, the concentration of bicarbonate close to the surface is higher than in the bulk. The curves decay very similarly and for more than 15 s the pH stays at around 6. At the more negative sample potentials, in which carbonate is also formed in higher concentrations, the pH drops to 6 within 5 s, and then gradually decreases to the bulk value. These observations are a consequence of both how fast the different species formed as a function of pH diffuse in the electrolyte and the rate of the different homogeneous reactions taking place in CO_2 atmosphere. Figure 4c shows a schematic representation of the reactions taking place at the sample surface and in solution. If only HER takes place (argon atmosphere), even though the interfacial pH reaches relatively higher values, the recovery of the diffusion layer happens fast. This is a consequence of the high diffusion coefficient of the species involved in the reaction ($D_{H^+} = 9.31 \cdot 10^{-5}$ cm^2 s^{-1} and $D_{H^-} = 5.27 \cdot 10^{-5}$ cm^2 s^{-1}) and of the absence of any additional buffer system. In contrast, in CO_2 atmosphere, bicarbonate and carbonate are formed, whose concentrations are a function of pH. These are much slower diffusing species ($D_{HCO_3^-} = 1.18 \cdot 10^{-5}$ cm^2 s^{-1} and $D_{CO_3^{2-}} = 0.95 \cdot 10^{-5}$ cm^2 s^{-1}). Additionally, the reversible reaction of $CO_3^{2-} \rightarrow HCO_3^-$ is fast while the $HCO_3^- \rightarrow CO_2$ reaction is much slower (see values in Table S2 in the Supporting Information). As a consequence, the pH decays fast toward the pK_a of the CO_2/HCO_3^- equilibrium, but afterward, it takes more than 40 s to reach the bulk pH value. These observations have strong implications for experiments in electrocatalysis. For instance, if one wishes to perform several measurements in a row, enough time must be given to the system (without any reaction taking place) in order to restore the bulk pH at the interface. Furthermore, we provide here a tool for probing such equilibrium reactions under operando conditions, which is relevant not only for CO_2 reduction but also for other electrocatalytic systems.

Finite Element Method (FEM) Simulations

In SECM, it is known that the tip may physically block the diffusion of species and alter their concentrations in the diffusion layer, thus influencing the pH measurement.[32] In order to account for this effect, we have simulated the experimental results presented in Figure 3 (and summarized in Figure S6) using finite element method based modeling implemented in COMSOL Multiphysics. Fitted kinetic parameters and the use of a 2D axisymmetric model leads to good agreement between simulated and experimental results. This enables us to quantify the local pH excluding the effect of the SECM tip.

First, we considered the pH response during reactions taking place in argon atmosphere (Figure 3a), namely, proton reduction (PR) and water reduction (WR). The governing equations as well as the parameters and the fitting procedure used to obtain these parameters are discussed in detail in Figures S7−S10 and Table S1 and the SI. Here, we only summarize the main points: the PR rate is assumed to be linear in the proton concentration, as is the case if the Volmer step or a large-overpotential Heyrovsky step is rate limiting. This assumption is justified by the Tafel slope obtained from chronoamperometry being 147 mV/dec (see Figure S7)[33] The kinetic parameters for proton reduction, as well as the proton diffusion coefficient were obtained by fitting the cyclic voltammetry (Figure 2, argon), the result of which is shown in Figure S8. Subsequently, the pH-potential relation (Figure 3, argon) after 100s chronoamperometry was fit to obtain kinetic parameters for water reduction. For comparison to experiment, the pH values were thereby averaged over the SECM electrode area. Relevant diffusion coefficients (except the proton diffusion coefficient) and the rate constant for water association were thereby taken from literature (see Table S2).

The fitted parameters can be used to simulate the pH map during hydrogen evolution after 100 s chronoamperometry with and without tip present and hence to investigate the influence of the tip on the pH measurements. As an example, we show the pH map obtained at a substrate potential of −0.8 V vs Ag/AgCl with and without the probe tip positioned at 80 μm above the surface in Figure 5. The pH maps shown demonstrate that the tip significantly blocks diffusion of species away from the electrode surface. However, this effect is highly localized to the gap below the SECM tip; at horizontal positions far from the tip, the concentration profile approaches the "without tip" conditions.

Similar calculations can also be performed to estimate the influence the tip has on the transient chronoamperometry data. In Figure 6, we simulate the chronoamperometry data at 100 s with and without tip present (solid vs dashed line). The

https://doi.org/10.1021/jacsau.1c00289
JACS Au 2021, 1, 1915−1924

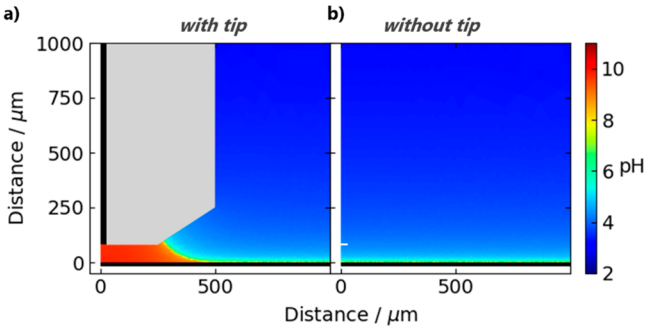

Figure 5. pH profile near the electrode surface during hydrogen evolution reaction (a) with and (b) without the SECM tip present. Sample potential applied −0.8 V vs Ag/AgCl.

concentration of protons estimated with the tip absent is significantly higher than that obtained with the tip present, especially at potentials between −0.65 and −0.85 V vs Ag/AgCl. At low overpotentials without the SECM tip present, the pH gradients are minimal. Only at large overpotentials will proton consumption at the surface electrode combined with increased hydroxide production due to the onset of water reduction cause the pH boundary layer to grow to a size comparable to the tip−surface separation (see Figure S10). In the presence of the SECM tip, hindered diffusion directly below the tip causes the pH to rise more gradually already at a much less reducing potential. The sudden rise in pH between overpotentials of −0.6 to −0.7 V vs Ag/AgCl can be ascribed to a switch from proton reduction to mainly water reduction, as shown in Figure S9 in the SI.

A similar analysis was performed for the measurement in CO_2 atmosphere (Figure 6b). (See eqs 12−17 for the governing electrochemical equations and Equations S1−S7 in the SI for the governing equations of the additional homogeneous equations. Table S2 lists the relevant parameters). Although no additional fit was performed, the simulation data (solid line) resembles the experimental results (red dots). Comparing panels a and b of Figure 6, it becomes clear that the pH measured in CO_2 atmosphere remains lower than that measured in argon atmosphere over the entire potential range. This is a consequence of the buffering effect of the CO_2 species present, as evidenced by the two plateau regions in the pH-potential relation, which correlate to the pK_a of bicarbonate (eq 6) and carbonate (eq 7). Although the buffering effect of the CO_2 species is most striking in the presence of the tip, the buffering of the electrolyte is also relevant in the absence of the tip. This is evidenced by the shift of the sudden increase in pH observed in argon atmosphere at −0.85 V to even more negative potentials (not plotted). The presence of CO_2 and its derivatives thus has a significant buffering effect near the electrode at experimentally relevant conditions in both the presence and the absence of the tip.

Hindering the diffusion and inducing a high local alkalinity at the reaction interface allowed us to study the diffusion layer during CO_2RR at relatively low sample potentials (and current densities), which circumvents, for example, bubble issues and allows for gradually modulating the pH below the tip. However, this tip blocking effect could of course be minimized by decreasing the radius of the tip insulating layer or by working at larger distances from the surface. Using calculations similar to those shown in Figure 6a, we have simulated the effect of decreasing the radius of the tip insulation on the pH response. Figure 7 shows the results of the FEM simulations carried out using different insulating radii from 20*R_{tip} (the experimental value, R_{tip} from the UME used in this work) down to 1.2*R_{tip}, for a constant tip−sample distance. The simulated pH response in the absence of the SECM tip is also plotted for comparison. It can be seen that for an ideal insulation layer radius of 1.2*R_{tip}, the calculated pH values closely approach those obtained without the tip present. When desired, this situation can be achieved, for example, by using a laser puller to produce the microelectrodes. However, it is important to point out that we find that obtaining a good sealing between the gold and the glass can be challenging, contrary to other metals that have a better adhesion to the insulation layer, like platinum. Alternatively, decreasing the radius of the tip (R_{tip}) will also decrease the diffusion hindrance and change the profiles shown in Figure 7.

Coupling SECM measurements with FEM simulations is a resourceful way to account for the physical blocking effect that the SECM probe has on interfacial concentration profiles. Our case is concerned with proton concentration, but the approach

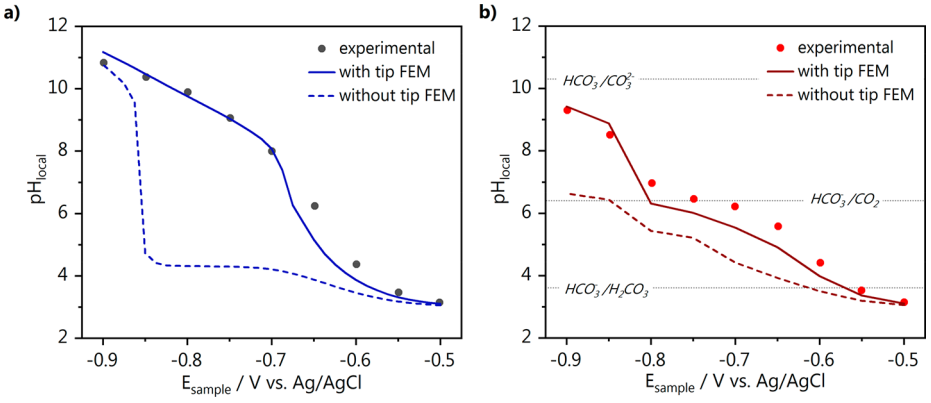

Figure 6. FEM modeling of the pH response measured with SECM. (a) Hydrogen evolution pH−potential comparison of experimental results in argon (black dots) and FEM simulation results (blue line) for L = 3.4 (close to the surface), compared to the case when the tip is far from the surface (L = 50, blue dashed line). The simulated pH "without tip" is obtained from a cross section at 80 μm from the surface with the tip removed to 1.25 mm from the surface (L = 50); L is the normalized tip−surface separation (see Experimental Section). (b) Similarly, experimental (red dots) and simulation (dark red line) pH under CO_2 reduction for L = 3.4 is compared to simulated L = 50 (dark red dashed line). Bulk CO_2 concentration was fixed at 10 mM.

https://doi.org/10.1021/jacsau.1c00289
JACS Au 2021, 1, 1915−1924

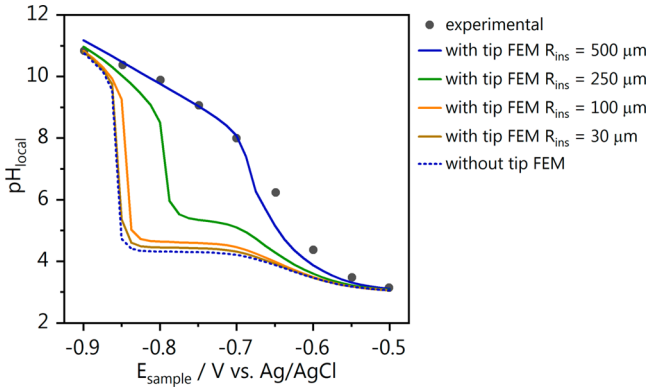

Figure 7. Minimization of tip effects by decreasing the insulation radius. Comparison is made for the experiment in argon, using the results from Figure 6a, and simulations decreasing the insulation radii, with a constant R_{tip}. The bottom tip insulation radius is maintained at 1/2 R_{ins} (see Figure 8 in the Experimental Section).

also applies to the detection of other species in solution, participating or not in a catalytic reaction. On the other hand, this hindrance of diffusion can also be intentionally introduced to induce a high local alkalinity in a controlled fashion and allow the study of homogeneous and inhomogeneous reactions taking place in the diffusion layer, as shown in this and our other recent work.[25]

CONCLUSION

Here, we have shown that our recently developed SECM pH sensor based on a 4-HATP/4-NSTP functionalized Au-UME is suitable for monitoring the pH in the diffusion layer during CO_2 reduction with high time resolution. We performed experiments using a polycrystalline gold substrate and monitored the pH as a function of potential at a fixed distance from the surface, in both argon and CO_2 atmospheres. Starting from bulk pH 3, we see a gradual increase in pH in argon as the potential applied is more negative, while in the presence of CO_2, a buffering region is present, keeping the pH around the pK_a of the $CO_2 \leftrightarrow HCO_3^-$ reversible reaction. By observing the time-dependent pH decay once the reaction at the sample is turned "off" as a function of applied potential, we probe how the local pH and the rate of the homogeneous reactions involving CO_2, HCO_3^-, CO_3^{2-} influence the time required to bring the diffusion layer pH back to the bulk value. Finally, we have accounted for the effect the SECM tip has on the measured pH by performing FEM simulations. We see how the presence of the tip leads to an overestimation of the local pH, due to the hindered diffusion of species generated by the substrate. Although in this work this hindered diffusion was intentional, we also show with FEM simulations to which extent this effect can be circumvented by, for example, decreasing the radius of the tip insulation layer.

EXPERIMENTAL SECTION

pH Sensor Fabrication

The functionalized gold pH sensor was fabricated by sealing a gold wire (50 μm diameter, H. Drijfhout en Zoon's Edelmetaal-bedrijven B.V.) in a glass capillary (0.4 mm i.d., Drummond Scientific Co.). The surface was prepared by grinding with a silicon carbide paper (grit size 600, MaTeck) followed by polishing the exposed cross section with diamond suspension for 2 min (1, 0.25, and 0.05 μm, MetaDi, Buehler). In between each polishing step the ultramicroelectrode (UME) was sonicated (Bandelin Sonorex RK 52H) in ultrapure water (>18.2 MΩ cm, Millipore Milli-Q) for 5 min. After the last polishing step, the UME was sonicated first in ethanol for 5 min than in water for 15 min. Due to the manual polishing, some degree of roughness is expected on the microelectrode surface. The gold UME was characterized in a one compartment electrochemical cell (20 mL). The blank voltammetry was taken in an argon-saturated 0.1 M H_2SO_4 electrolyte, with a gold wire as counter electrode (0.5 mm diameter, MaTeck, 99.9%) and a Ag/AgCl (LowProfile, Pine Research Instrumentation) reference electrode. After characterization, the gold UME was immersed in 1 mM of a 4-nitrothiophenol/ethanol (4-NTP, Merck, 80%) solution for 20 min. Next, the electrode was rinsed thoroughly with ethanol and transferred back to the cell where the characterization was performed. The 4-nitrothiophenol monolayer was electrochemically converted to the pH sensitive redox couple by polarization from 0.1 to −0.25 V vs Ag/AgCl at 100 mV s^{-1}. The voltammetry of the 4-nitrosothiophenol/4-hydroxiaminothiophenol redox couple was obtained in Li_2SO_4 (Sigma-Aldrich, 99.99%, metal basis) solutions of different pH in order to construct a calibration curve. This was done in both argon and CO_2 atmosphere by saturating the electrolyte for 5 min prior to each cyclic voltammetry measurement.

SECM Measurements

pH measurements were performed in a home-built SECM setup, which was described in our previous work.[29] The glass parts were cleaned prior to the experiment by immersion in potassium permanganate solution for 24 h (1 g L^{-1} $KMnO_4$ dissolved in 0.5 M H_2SO_4). Next, the glassware was immersed in dilute piranha solution and then boiled at least five times in ultrapure water. The sample was a polycrystalline gold disc (0.5 mm thick, MaTeck, 99.995%) prepared by polishing with diamond suspension and flame annealed as described in our previous work.[34] The tip-to-surface distance was determined by performing a capacitive approach in air.[25,29,31] An AC potential (4 V_{pp}, 10 kHz) was applied to the sample using a function generator (33210A, Keysight). The gold ultramicroelectrode was connected to a low noise current preamplifier (SR570, Stanford Research) operated at high bandwidth with a gain of 2×10^8 V A^{-1} and the capacitive tip current was obtained using a virtual lock-in amplifier (LabView). The approach curve was fitted with the following equation:

$$C_{tot}(Z) = -A_1 * \ln(d_0 - Z) + B + \left(\frac{A_2}{L_{par} + d_0 - Z}\right) \quad (9)$$

With the obtained fitting parameter d_0, the tip-to-surface distance is determined. A detailed explanation of the approach method is described in our previous work.[25,29]

The pH measurements were performed in six-electrode configuration, with the sample and the tip controlled by two different potentiostat channels. The cell was filled with 5 mL of electrolyte (0.1 M Li_2SO_4, pH = 3), which during the measurements was constantly purged through and above the solution with argon or CO_2. Working with Li_2SO_4 at a mildly acidic pH allows us to probe the reactions at a wide potential range, due to the low activity for CO_2 reduction and hydrogen evolution in this electrolyte.[35] During the pH measurements, the tip was kept at a fixed distance from the surface and either hydrogen evolution or CO_2 reduction were turned "on" and "off" at the sample. The tip voltammetry was continuously recorded (200 mV s^{-1}) and the midpeak potential of each cycle was obtained by fitting it with a Gaussian function with a linear background. The midpeak potential was converted to pH using the relationship obtained from the calibration curve, pH = (0.341 − E_{peak})/0.057.

Finite Element Method (FEM) Simulation

The experimental system is represented by a 2D axisymmetric cylindrical SECM tip and a planar working electrode at the bottom of a cylindrical cell. Geometric parameters[29] are listed in Table 1 with a graphical depiction of the geometry in Figure 8.

https://doi.org/10.1021/jacsau.1c00289
JACS Au 2021, 1, 1915−1924

Table 1. Geometric Parameters

parameter	value
tip radius (R_{tip}, μm)	25
insulation radius (R_{ins}, μm)	500
working electrode radius (R_{sub}, mm)	5
boundary radius (R_{bound}, mm)	8
normalized tip−surface separation (L)	3.4
tip electrode height (h_{ins}, mm)	7.4

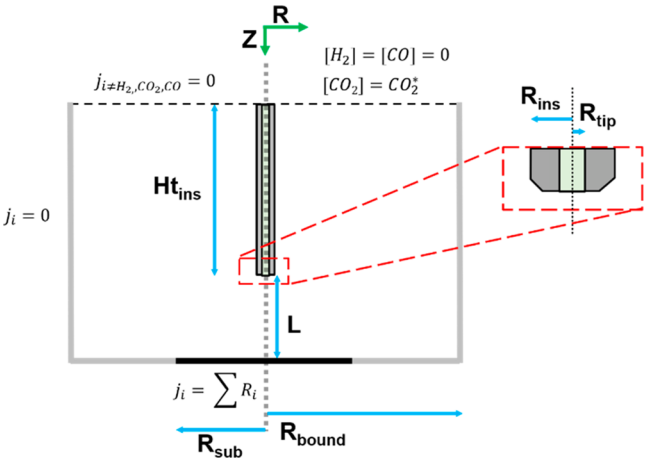

Figure 8. Geometric description of the experimental system with simulation boundary conditions used for hydrogen evolution and CO_2 reduction.

Migration is neglected and transport is governed by Fick's second law of diffusion. Proton-hydroxide ion recombination is included as a homogeneous reaction along with the carbon dioxide reversible reactions (eqs 4−7). The governing equations are

$$\frac{dC_i}{dt} = D_i\nabla^2 C_i + \sum R_{ij} \tag{10}$$

where C_i is the concentration of each species in solution (H^+, OH^-, H_2O, H_2, Li^+, and SO_4^{2-}), D_i is the species diffusion coefficient, and the reversible reaction rates, R_{ij}, for each species, i, are summed for each reversible reaction, j.

The boundary conditions, visually represented in Figure 8, are as follows: At the WE surface ($z = 0$), a flux balance is applied using the electrode reaction:

$$-D\nabla C_i\cdot\vec{n} = \sum_j r_{ij} \tag{11}$$

where $\vec{n}$ is the surface normal. The summation is over all surface reactions, j, and r_{ij} is the rate of production of species i due to reaction j; $\sum r_{ij}$ is the summation of the reactions involving a given species, i. Proton reduction (PR), water reduction (WR) and carbon dioxide reduction (CO2R, eq 14) are considered at the substrate. Proton reduction and water reduction rates are assumed to be limited by Volmer adsorption of hydrogen (eqs 12 and 13, respectively, E_{app} is an arbitrary reference potential for the first reaction step).[33,36]

$$\text{PR, Volmer step: } H^+ + S + e^- \overset{k_{0,PR}}{\longleftrightarrow} H_{ads}$$
$$E_{app} = 0\text{ V vs SHE at pH} = 0 \tag{12}$$

$$\text{WR, Volmer step: } H_2O + S + e^- \overset{k_{0,WR}}{\longleftrightarrow} OH^- + H_{ads}$$
$$E_{app} = 0\text{ V vs SHE at pH} = 0 \tag{13}$$

$$CO_2RR:\ CO_2 + H_2O + 2e^- \overset{k_{0,CO_2R}}{\longleftrightarrow} 2OH^- + CO$$
$$E_0 = -0.52\text{ V vs SHE at pH} = 7 \tag{14}$$

The rates of PR and WR, due to the large overpotentials, were expressed by Tafel kinetics. CO_2RR was expressed in Butler−Volmer form:

$$r_{PR} = k_{0,PR}(C_{H^+}\exp(-\alpha_{PR}n_{PR}f\eta_{PR})) \tag{15}$$

$$r_{WR} = k_{0,WR}(C_{H_2O}\exp(-\alpha_{WR}n_{WR}f\eta_{WR})) \tag{16}$$

$$r_{CO_2RR} = k_{0,CO_2RR}(C_{CO_2RR}C_{H^+}^2\exp(-\alpha_{CO_2RR}n_{CO_2R}f\eta_{CO_2RR}) - C_{H_2O}C_{CO}\exp((1-\alpha_{CO_2RR})n_{CO_2RR}f\eta_{CO_2RR})) \tag{17}$$

where $k_{0,j}$ are the rate constants, the number of electrons is n_j, the charge transfer coefficient is α_j, and $\eta_j = E - E_{0,j}$, where the $E_{0,j}$ are the formal potentials and E is the applied surface potential. Finally, $f = \frac{F}{RT}$, where F is Faraday's constant, R is the gas constant, and T is the temperature.

Three surface reactions occur simultaneously at the gold surface electrode. At the liquid-atmosphere boundary ($z = L + ht_{ins}$), the concentration of molecular hydrogen, H_2, is zero (Figure 3), the bulk concentration of CO_2 is set to 0 (under Ar) or 10 mM (under CO_2), and flux is set to zero for all other species. This bulk CO_2 concentration, which is roughly half of the estimated saturation concentration (23 mM, for 1 atm CO_2 in 0.1 M Li_2SO_4 at pH 3 and 25 C), is set to avoid numerical convergence issues encountered at higher concentrations.

At all other boundaries, a zero-flux condition is imposed for all species. Diffusivities used in the simulation are listed in Table S1 with the equilibrium and dissociation constants for the reversible reactions. Kinetic rate constants for the homogeneous dissociation reactions were obtained from Wuttig et al.[37] and Bohra et al.[38] The tip electrode proton adsorption is assumed to have negligible effects on the pH.

■ ASSOCIATED CONTENT

Supporting Information

The Supporting Information is available free of charge at https://pubs.acs.org/doi/10.1021/jacsau.1c00289.

Characterization of the Au-UME, calibration CVs, SECM approach curves, sample chronoamperometry, finite element method parameters (PDF)

■ AUTHOR INFORMATION

Corresponding Author

Marc T. M. Koper − *Leiden Institute of Chemistry, Leiden University, 2300 RA Leiden, The Netherlands;* orcid.org/0000-0001-6777-4594; Email: m.koper@lic.leidenuniv.nl

Authors

Mariana C. O. Monteiro − *Leiden Institute of Chemistry, Leiden University, 2300 RA Leiden, The Netherlands;* orcid.org/0000-0001-7451-1004

Alex Mirabal − *Department of Chemical & Materials Engineering, Michigan State University, East Lansing, Michigan 48824, United States;* orcid.org/0000-0002-4501-7602

Leon Jacobse − *Centre for X-ray and Nano Science CXNS, Deutsches Elektronen-Synchrotron DESY, D-22607 Hamburg, Germany;* orcid.org/0000-0002-2825-0963

https://doi.org/10.1021/jacsau.1c00289
JACS Au 2021, 1, 1915−1924

Katharina Doblhoff-Dier − *Leiden Institute of Chemistry, Leiden University, 2300 RA Leiden, The Netherlands;* orcid.org/0000-0002-5981-9438

Scott Calabrese Barton − *Department of Chemical & Materials Engineering, Michigan State University, East Lansing, Michigan 48824, United States;* orcid.org/0000-0002-1407-0275

Complete contact information is available at: https://pubs.acs.org/10.1021/jacsau.1c00289

Author Contributions

The manuscript was written through contributions of all authors. All authors have given approval to the final version of the manuscript.

Notes

The authors declare no competing financial interest.

■ ACKNOWLEDGMENTS

This work was supported by the European Commission under contract 722614 (Innovative training network Elcorel).

■ REFERENCES

(1) Kortlever, R.; Shen, J.; Schouten, K. J. P.; Calle-Vallejo, F.; Koper, M. T. M. Catalysts and Reaction Pathways for the Electrochemical Reduction of Carbon Dioxide. *J. Phys. Chem. Lett.* **2015**, *6* (20), 4073−4082.

(2) Bagger, A.; Ju, W.; Varela, A. S.; Strasser, P.; Rossmeisl, J. Electrochemical CO 2 Reduction: A Classification Problem. *ChemPhysChem* **2017**, *18* (22), 3266−3273.

(3) Yu, F.; Wei, P.; Yang, Y.; Chen, Y.; Guo, L.; Peng, Z. Material Design at Nano and Atomic Scale for Electrocatalytic CO2 Reduction. *Nano Mater. Sci.* **2019**, *1* (1), 60−69.

(4) Vennekötter, J.-B.; Scheuermann, T.; Sengpiel, R.; Wessling, M. The Electrolyte Matters: Stable Systems for High Rate Electrochemical CO_2 Reduction. *J. CO2 Util.* **2019**, *32*, 202−213.

(5) Moura de Salles Pupo, M.; Kortlever, R. Electrolyte Effects on the Electrochemical Reduction of CO_2. *ChemPhysChem* **2019**, *20* (22), 2926−2935.

(6) Kas, R.; Kortlever, R.; Yılmaz, H.; Koper, M. T. M.; Mul, G. Manipulating the Hydrocarbon Selectivity of Copper Nanoparticles in CO_2 Electroreduction by Process Conditions. *ChemElectroChem* **2015**, *2* (3), 354−358.

(7) Varela, A. S.; Kroschel, M.; Reier, T.; Strasser, P. Controlling the Selectivity of CO2 Electroreduction on Copper: The Effect of the Electrolyte Concentration and the Importance of the Local PH. *Catal. Today* **2016**, *260*, 8−13.

(8) Marcandalli, G.; Goyal, A.; Koper, M. T. M. Electrolyte Effects on the Faradaic Efficiency of CO_2 Reduction to CO on a Gold Electrode. *ACS Catal.* **2021**, *11*, 4936−4945.

(9) Schouten, K. J. P.; Pérez Gallent, E.; Koper, M. T. M. The Influence of PH on the Reduction of CO and CO 2 to Hydrocarbons on Copper Electrodes Dedicated to Professor Kingo Itaya on the Occasion of His 65th Birthday and in Recognition of His Seminal Contributions to Physical Electrochemistry. *J. Electroanal. Chem.* **2014**, *716*, 53−57.

(10) Varela, A. S.; Kroschel, M.; Leonard, N. D.; Ju, W.; Steinberg, J.; Bagger, A.; Rossmeisl, J.; Strasser, P. PH Effects on the Selectivity of the Electrocatalytic CO2 Reduction on Graphene-Embedded Fe-N-C Motifs: Bridging Concepts between Molecular Homogeneous and Solid-State Heterogeneous Catalysis. *ACS Energy Lett.* **2018**, *3* (4), 812−817.

(11) Raciti, D.; Mao, M.; Park, J. H.; Wang, C. Local PH Effect in the CO2 Reduction Reaction on High-Surface-Area Copper Electrocatalysts. *J. Electrochem. Soc.* **2018**, *165* (10), F799−F804.

(12) Resasco, J.; Chen, L. D.; Clark, E.; Tsai, C.; Hahn, C.; Jaramillo, T. F.; Chan, K.; Bell, A. T. Promoter Effects of Alkali Metal Cations on the Electrochemical Reduction of Carbon Dioxide. *J. Am. Chem. Soc.* **2017**, *139* (32), 11277−11287.

(13) Thorson, M. R.; Siil, K. I.; Kenis, P. J. A. Effect of Cations on the Electrochemical Conversion of CO_2 to CO. *J. Electrochem. Soc.* **2013**, *160* (1), F69−F74.

(14) Ringe, S.; Clark, E. L.; Resasco, J.; Walton, A.; Seger, B.; Bell, A. T.; Chan, K. Understanding Cation Effects in Electrochemical CO2 Reduction. *Energy Environ. Sci.* **2019**, *12* (10), 3001−3014.

(15) Pérez-Gallent, E.; Marcandalli, G.; Figueiredo, M. C.; Calle-Vallejo, F.; Koper, M. T. M. Structure- and Potential-Dependent Cation Effects on CO Reduction at Copper Single-Crystal Electrodes. *J. Am. Chem. Soc.* **2017**, *139* (45), 16412−16419.

(16) Hong, S.; Lee, S.; Kim, S.; Lee, J. K.; Lee, J. Anion Dependent CO/H 2 Production Ratio from CO 2 Reduction on Au Electro-Catalyst. *Catal. Today* **2017**, *295* (July), 82−88.

(17) Resasco, J.; Lum, Y.; Clark, E.; Zeledon, J. Z.; Bell, A. T. Effects of Anion Identity and Concentration on Electrochemical Reduction of CO2. *ChemElectroChem* **2018**, *5* (7), 1064−1072.

(18) Goyal, A.; Marcandalli, G.; Mints, V. A.; Koper, M. T. M. Competition between CO_2 Reduction and Hydrogen Evolution on a Gold Electrode under Well-Defined Mass Transport Conditions. *J. Am. Chem. Soc.* **2020**, *142* (9), 4154.

(19) Schulz, K. G.; Riebesell, U.; Rost, B.; Thoms, S.; Zeebe, R. E. Determination of the Rate Constants for the Carbon Dioxide to Bicarbonate Inter-Conversion in PH-Buffered Seawater Systems. *Mar. Chem.* **2006**, *100* (1−2), 53−65.

(20) Monteiro, M. C. O.; Koper, M. T. M. Measuring Local PH in Electrochemistry. *Curr. Opin. Electrochem.* **2021**, *25*, 100649.

(21) Yang, K.; Kas, R.; Smith, W. A. In Situ Infrared Spectroscopy Reveals Persistent Alkalinity near Electrode Surfaces during CO_2 Electroreduction. *J. Am. Chem. Soc.* **2019**, *141* (40), 15891−15900.

(22) Ayemoba, O.; Cuesta, A. Spectroscopic Evidence of Size-Dependent Buffering of Interfacial PH by Cation Hydrolysis during CO_2 Electroreduction. *ACS Appl. Mater. Interfaces* **2017**, *9* (33), 27377−27382.

(23) Zhang, Z.; Melo, L.; Jansonius, R. P.; Habibzadeh, F.; Grant, E. R.; Berlinguette, C. P. PH Matters When Reducing CO_2 in an Electrochemical Flow Cell. *ACS Energy Lett.* **2020**, *5* (10), 3101−3107.

(24) Zhang, F.; Co, A. C. Direct Evidence of Local PH Change and the Role of Alkali Cation during CO 2 Electroreduction in Aqueous Media. *Angew. Chem., Int. Ed.* **2020**, *59* (4), 1674−1681.

(25) Monteiro, M. C. O.; Jacobse, L.; Koper, M. T. M. Understanding the Voltammetry of Bulk CO Electrooxidation in Neutral Media through Combined SECM Measurements. *J. Phys. Chem. Lett.* **2020**, *11* (22), 9708−9713.

(26) García, G. Correlation between CO Oxidation and H Adsorption/Desorption on Pt Surfaces in a Wide PH Range: The Role of Alkali Cations. *ChemElectroChem* **2017**, *4* (3), 459−462.

(27) Gisbert, R.; García, G.; Koper, M. T. M. Oxidation of Carbon Monoxide on Poly-Oriented and Single-Crystalline Platinum Electrodes over a Wide Range of PH. *Electrochim. Acta* **2011**, *56* (5), 2443−2449.

(28) Dieckhöfer, S.; Öhl, D.; Junqueira, J. R. C.; Quast, T.; Turek, T.; Schuhmann, W. Probing the Local Reaction Environment During High Turnover Carbon Dioxide Reduction with Ag-Based Gas Diffusion Electrodes. *Chem. - Eur. J.* **2021**, *27* (19), 5906−5912.

(29) Monteiro, M. C. O.; Jacobse, L.; Touzalin, T.; Koper, M. T. M. Mediator-Free SECM for Probing the Diffusion Layer PH with Functionalized Gold Ultramicroelectrodes. *Anal. Chem.* **2020**, *92* (2), 2237−2243.

(30) Touzalin, T. *Tip-Enhanced Raman Spectroscopy on Electrochemical Systems*; Sorbonne Université, 2018.

(31) de Voogd, J.M.; van Spronsen, M.A.; Kalff, F.E.; Bryant, B.; Ostojic, O.; den Haan, A.M.J.; Groot, I.M.N.; Oosterkamp, T.H.; Otte, A.F.; Rost, M.J. Fast and Reliable Pre-Approach for Scanning

Probe Microscopes Based on Tip-Sample Capacitance. *Ultramicroscopy* **2017**, *181*, 61−69.
(32) Critelli, R. A. J.; Bertotti, M.; Torresi, R. M. Probe Effects on Concentration Profiles in the Diffusion Layer: Computational Modeling and near-Surface PH Measurements Using Microelectrodes. *Electrochim. Acta* **2018**, *292*, 511−521.
(33) Shinagawa, T.; Garcia-Esparza, A. T.; Takanabe, K. Insight on Tafel Slopes from a Microkinetic Analysis of Aqueous Electrocatalysis for Energy Conversion. *Sci. Rep.* **2015**, *5* (1), 13801.
(34) Monteiro, M. C. O.; Koper, M. T. M. Alumina Contamination through Polishing and Its Effect on Hydrogen Evolution on Gold Electrodes. *Electrochim. Acta* **2019**, *325*, 134915.
(35) Monteiro, M. C. O.; Dattila, F.; Hagedoorn, B.; Garcia-Muelas, R.; Lopez, N.; Koper, M. T. M. Absence of CO2 Electroreduction on Copper, Gold and Silver Electrodes without Cations in Solution. *Nat. Catal.* **2021**, *4*, 654.
(36) Carneiro-Neto, E. B.; Lopes, M. C.; Pereira, E. C. Simulation of Interfacial PH Changes during Hydrogen Evolution Reaction. *J. Electroanal. Chem.* **2016**, *765*, 92−99.
(37) Wuttig, A.; Yoon, Y.; Ryu, J.; Surendranath, Y. Bicarbonate Is Not a General Acid in Au-Catalyzed CO_2 Electroreduction. *J. Am. Chem. Soc.* **2017**, *139* (47), 17109−17113.
(38) Bohra, D.; Chaudhry, J. H.; Burdyny, T.; Pidko, E. A.; Smith, W. A. Modeling the Electrical Double Layer to Understand the Reaction Environment in a CO_2 Electrocatalytic System. *Energy Environ. Sci.* **2019**, *12* (11), 3380−3389.

https://doi.org/10.1021/jacsau.1c00289
JACS Au 2021, 1, 1915−1924